Remarkable NIR Enhancement of Multifunctional Nanoprobes for In Vivo Trimodal Bioimaging and Upconversion Optical/T_2-Weighted MRI-Guided Small Tumor Diagnosis

Zhigao Yi, Xiaolong Li, Zhenluan Xue, Xiao Liang, Wei Lu, Hao Peng, Hongrong Liu, Songjun Zeng, and Jianhua Hao**

Effective nanoprobes and contrast agents are urgently sought for early-stage cancer diagnosis. Upconversion nanoparticles (UCNPs) are considerable alternatives for bioimaging, cancer diagnosis, and therapy. Yb^{3+}/Tm^{3+} co-doping brings both emission and excitation wavelengths into the near-infrared (NIR) region, which is known as "optical transmission window" and ideally suitable for bioimaging. Here, NIR emission intensity is remarkably enhanced by 113 times with the increase of Yb^{3+} concentration from 20% to 98% in polyethylene glycol (PEG) modified $NaYF_4$:Yb^{3+}/Tm^{3+} UCNPs. PEG-UCNPs-5 (98% Yb^{3+}) can act as excellent nanoprobes and contrast agents for trimodal upconversion (UC) optical/CT/T_2-weighted magnetic resonance imaging (MRI). In addition, the enhanced detection of lung in vivo long-lasting tracking, as well as possible clearance mechanism and excretion routes of PEG-UCNPs-5 have been demonstrated. More significantly, a small tumor down to 4 mm is detected in vivo via intravenous injection of these nanoprobes under both UC optical and T_2-weighted MRI modalities. PEG-UCNPs-5 can emerge as bioprobes for multi-modal bioimaging, disease diagnosis, and therapy, especially the early-stage tumor diagnosis.

1. Introduction

In vivo optical bioimaging is one of the most efficient and widely used imaging technologies. Luminescent bioprobes have been rapidly developed for optical imaging in recent years, especially the one on the basis of upconversion (UC) process.[1–16] Upconversion nanoparticles (UCNPs) are considered as a next generation of nanoprobes for in vivo optical bioimaging owing to their unique merits, such as low biotoxicity, excellent UC emission, minimized autofluorescence, deep penetration depth, etc.[17–25] In general, the well-established Yb^{3+}/Er^{3+} and Yb^{3+}/Ho^{3+} systems present dominant green emission under the 980 nm excitation.[26–29] However, UC emission located in short wavelengths within visible spectrum is not optimal for in vivo bioimaging owing to appreciable absorption of bio-tissues, although the Mn^{2+} doping method can realize an enhanced red emission in Yb^{3+}/Er^{3+} co-doped $NaLnF_4$ systems

Z. G. Yi, X. L. Li, Z. L. Xue, Prof. H. R. Liu, Prof. S. J. Zeng
College of Physics and Information Science and Key Laboratory of Low-Dimensional Quantum Structures and Quantum Control of the Ministry of Education
Hunan Normal University
Changsha 410081, China
E-mail: songjunz@hunnu.edu.cn

Z. G. Yi
School of Materials Science and Engineering
Key Laboratory of Low-Dimensional Materials and Application Technology (Ministry of Education)
Xiangtan University
Xiangtan 411105, China

X. Liang
Key Laboratory of Molecular Imaging of Chinese Academy of Sciences
Institute of Automation
Chinese Academy of Sciences
Beijing 100190, China

Dr. W. Lu, Prof. J. H. Hao
Department of Applied Physics and Materials Research Center
The Hong Kong Polytechnic University
Hong Kong, China
E-mail: jh.hao@polyu.edu.hk

H. Peng
Research Center of Heart Development
School of Life Sciences
Hunan Normal University
Changsha, Hunan 410081, China

DOI: 10.1002/adfm.201503672

reported by our previous report and other group.[30,31] $NaYF_4$:Yb^{3+}/Tm^{3+} UCNPs have triggered particular interest for their efficient NIR-to-NIR UC process, where both of the excitation and emission wavelengths are within 750–1000 nm, which is well known as "optical transmission window."[32,33] Compared with NIR-to-visible emission, NIR-to-NIR process efficiently prevents the emitted photon energy from endogenous absorption and therefore achieves a deeper penetration depth with high sensitivity.

More significantly, the intense and sensitive NIR emission of Yb^{3+}/Tm^{3+} co-doped UCNPs makes in vivo long-lasting tracking and biodistribution based on UC optical bioimaging possible. The efficient NIR-to-NIR process is suitable for deep tissue imaging and long-term in vivo biodistribution investigation, which can provide vital information for pharmacology/toxicology and diagnosis/therapy of nanoparticles. Recently, it is reported that NIR emission enhancement in $NaYF_4$:Yb^{3+}/Tm^{3+} system was realized through increasing the doping concentration of Yb^{3+} by thermal decomposition.[32] However, the rigorous conditions of synthesis (high temperature and inert gas protection) and additionally hydrophilic converting restrained further applications of these UCNPs for bioimaging and tumor detection. Therefore, it is desirable to develop a simple method and achieve the synthesis of hydrophilic UCNPs with efficient NIR-to-NIR emission for demonstrating long-term in vivo imaging and tumor diagnosis.

Apart from the significantly enhanced UC emission, the introduction of Yb^{3+} into host lattice brings additional imaging functions, namely X-ray computed tomography (CT) and T_2-weighted MRI. Yb^{3+}-based UCNPs can emerge as CT contrast agents owing to the large K-edge value (61 keV) and high X-ray absorption coefficient (6.91 cm^2 g^{-1} at 80 keV) of Yb^{3+}.[34,35] CT imaging provides accurate 3D information of tissues and high contrast, contributing to determining the location of the lesion,[36,37] while MRI becomes an increasingly significant approach to noninvasive tumor diagnosis for its high resolution of soft tissues. A number of MRI contrast agents have been explored to shorten longitudinal or transverse relaxation time of surrounding water protons to improve imaging contrast.[38–40] Among them, superparamagnetic iron oxide nanoparticles (SPIONs) have been used as widely applied T_2-weighted contrast agents owing to their high feasibility of detecting the lesion in T_2-weighted MRI.[41] Nevertheless, the magnetic susceptibility artifacts of SPIONs hinder their visualization and distinguishing sensitivity of tumor, especially when signal-to-noise ratio is low. Therefore, the development of multifunctional UCNPs offers the possibility to overcome the shortcomings from each single imaging modality and hence enhances the diagnosis efficiency. The short electronic transverse relaxation time and large intrinsic magnet moment (μ_{eff} = 4.53 μ_B) of Yb^{3+} make Yb^{3+}-hosted UCNPs can act as promising candidates for T_2-weighted MRI.[38] To the best of our knowledge, multifunctional Yb^{3+}-based UCNPs with remarkably enhanced NIR emission for trimodal UC optical/CT/T_2-weighted MRI have not been exploited yet. Moreover, the excellent optical and paramagnetic capabilities of these UCNPs inspire us to pursue tiny tumor detection under UC optical and MRI modalities, which is vital to diagnosis and therapy of early-stage cancer.

In this work, PEGylated $NaYF_4$:x%Yb^{3+}/2%Tm^{3+} (x = 20, 40, 60, 80, and 98) UCNPs (denoted as PEG-UCNPs-1, -2, -3, -4, and -5) were synthesized via a simple one-pot hydrothermal method using PEG as capping ligands. The effect of Yb^{3+} concentration on NIR emission intensity was studied. PEG-UCNPs-5 with strongest NIR emission was used for in vitro deep tissue penetration, trimodal UC optical/CT/T_2-weighted MRI bioimaging, long-circulation tracking, and UC optical/T_2-weighted MRI directed small tumor detection. In vivo UC whole body imaging based on blood circulation was performed to validate the merits of NIR emission. Long-term in vivo and ex vivo tracking of the injected PEG-UCNPs-5 was observed in real time to study the biodistribution and excretion mechanism of PEG-UCNPs-5. Moreover, in vivo detection of small tumor was also successfully achieved under UC optical/T_2-weighted MRI modalities, indicating that the designed PEG-UCNPs-5 molecular probes can be used as ideal agents for further biological and preclinical investigation, especially early-stage cancer diagnosis.

2. Results and Discussion

2.1. Phase and Microstructure Characterization

PEG-UCNPs-1, -2, -3, -4, and -5 were simultaneously synthesized and surface modified via a simple one-pot hydrothermal method using PEG as a surface modifier. As shown in **Figure 1**a, the diffraction peaks of PEG-UCNPs-1, -3, and -5 present the major cubic and weak hexagonal phases, which can match those of the standard cubic phase $NaYF_4$ (JCPDS file no. 77-2042) and hexagonal phase $NaYbF_4$ (JCPDS file no. 16-0334), respectively. No other extra peaks appear. When increasing Yb^{3+} doping concentrations, the phase compositions of these UCNPs are not evidently changed. As demonstrated by typical field-emission scanning electron microscope (FE-SEM) images (Figure S1, Supporting Information), all these PEGylated UCNPs are of nanoparticle shapes. The size distribution based on transmission electron microscopy (TEM) image (Figure 1c) of PEG-UCNPs-5 was measured to be 55.8 ± 9.1 nm (Figure S2, Supporting Information). The high-resolution TEM (HR-TEM) image shows a single nanoparticle of PEG-UCNPs-5 (Figure 1d), in which an interplanar spacing was nearly 3.08 Å, matching well with the (111) lattice plane of the cubic phase $NaYbF_4$. In addition, the selected area electron diffraction (SAED) pattern of PEG-UCNPs-5 (Figure 1e) presents the intense diffraction fringes of cubic phase, indicating that the cubic phase is dominant, which coincides with the former X-ray diffraction (XRD) analysis. The energy-dispersive X-ray spectrometer (EDS) analysis of PEG-UCNPs-5 (Figure 1f) demonstrates the mainly composed elements of Na, Yb, F, and Tm, further indicating the formation of $NaYbF_4$:Tm^{3+} UCNPs. Note that the detected Cu signal is ascribed to the TEM grid. The surface functional groups of PEG-UCNPs-5 and UCNPs without coating PEG were measured by Fourier transform infrared (FTIR) spectra, respectively. As presented by red curve in Figure 1b, the broad and strong stretching vibration band centered at 3436 cm^{-1} and peaks centered at 1364 cm^{-1} are corresponding to the O—H group and the C—O—C antisymmetric stretching, respectively. The characteristic peak centered at 1589 cm^{-1} originates from the C=O groups. The peak centered at 2823 cm^{-1} is assigned to the symmetric stretching

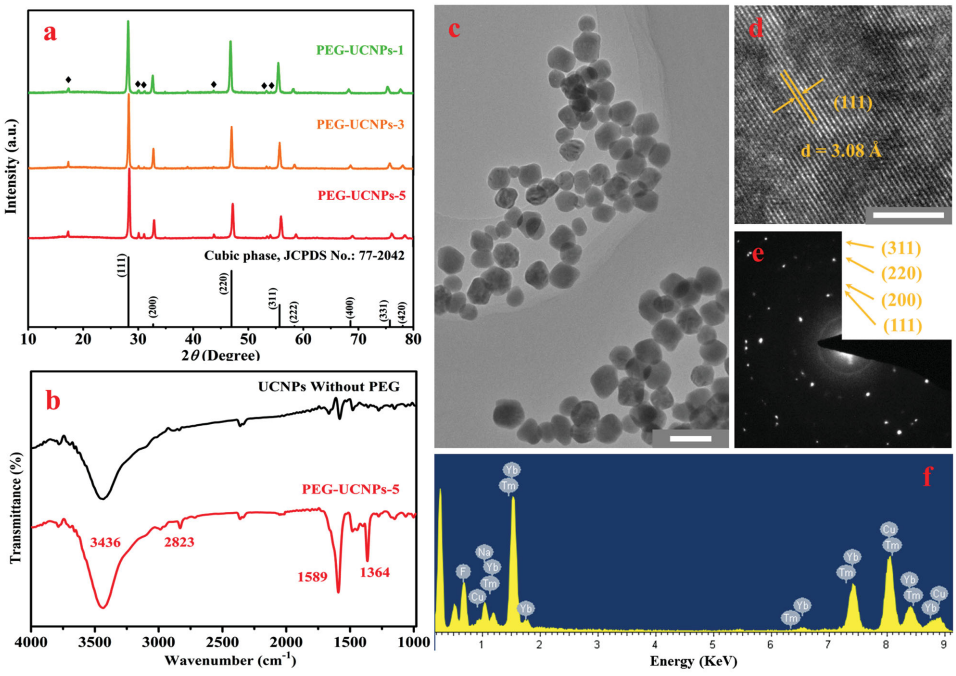

Figure 1. a) The XRD patterns of PEG-UCNPs-1, -3, and -5; b) FTIR spectra of PEG-UCNPs-5 and UCNPs without coating of PEG; c) TEM, d) HR-TEM, e) SAED, f) EDS of PEG-UCNPs-5. Scale bars are 100 nm for (c) and 5 nm for (d).

of $-CH_2$. The peak at 1507 cm^{-1} is due to the asymmetric (δ_{as}) $-COO^-$ stretching.[42] The FTIR results indicate that PEG is successfully coated onto the surface of these nanoparticles.

2.2. Remarkable Enhancement of NIR Emission

The UC emission spectra of these UCNPs (**Figure 2**a) present four distinct emission bands centered at 475, 650, 695, and 800 nm, which coincides with the $^1G_4 \rightarrow {}^3H_6$, $^1G_4 \rightarrow {}^3F_4$, $^3F_{2,3} \rightarrow {}^3H_6$, and $^3H_4 \rightarrow {}^3H_6$ transitions of Tm^{3+} (Figure 2b), respectively.[32] The predominant emission of these UCNPs locates within NIR region, which is favorable for in vivo UC optical bioimaging. Moreover, as seen in Figure 2c, the UC emission intensity centered at 800 nm increases by 4.3, 7.1, 14.7, and 113 times while Yb^{3+} concentration changes from 20% to 40%, 60%, and 98%, respectively. The NIR emission intensity enhancement is largely ascribed to the fact that the energy transfer efficiency increases with the increase in number of Yb^{3+} per Tm^{3+} and corresponding decrease in average distance between Yb^{3+} and Tm^{3+}.[32] The increased Yb^{3+} concentration facilities the energy transfer between Yb^{3+} and Tm^{3+}. However, the back-energy-transfer process $^1G_4$ (Tm^{3+}) + $^2F_{7/2}$ (Yb^{3+}) $\rightarrow$ $^3H_5$ (Tm^{3+}) + $^2F_{5/2}$ (Yb^{3+}) from Tm^{3+} to Yb^{3+} is meanwhile facilitated, which has an inhibitory effect on the population of $^1G_4$ (Tm^{3+}), resulting in the increase of the state $^3H_5$ (Tm^{3+}).[43] Therefore, the state $^3F_4$ (Tm^{3+}) is populated owing to the increased nonradiative transition from $^3H_5$ (Tm^{3+}). Consequently, through the energy transfer $^2F_{5/2}$ (Yb^{3+}) + $^3F_4$ (Tm^{3+}) $\rightarrow$ $^2F_{7/2}$ (Yb^{3+}) + $^3F_2$ (Tm^{3+}), the state $^3H_4$ (Tm^{3+}) can be directly populated because of the nonradiative relaxation of $^3F_2$ (Tm^{3+}), which leads to the significant enhancement in NIR emission centered at 800 nm. Apart from the effect of the dopant concentration, it is expected that the effects of the intrinsical larger probability of the phonon assisted energy transfer induced NIR emission and the phonons of the host matrix may contribute to the remarkably enhanced NIR-to-NIR emission.[44] In addition, in vitro UC imaging using the 96-well plates (inset in Figure 2d) also presents the remarkably enhanced NIR emission. As illustrated in Figure 2d, the value of signal to noise ratio (SNR) gradually increases from 4.7 to 68.1 and finally to 505.6, corresponding to PEG-UCNPs-1, -4, -5, respectively. UC emission spectra and in vitro UC imaging simultaneously verify that NIR emission can be dramatically promoted by increasing Yb^{3+} concentration and PEG-UCNPs-5 can act as promising luminescent nanoprobes for in vivo UC bioimaging.

Before using PEG-UCNPs-5 as bioprobes for in vivo bioimaging, the evaluation of cell toxicity of these UCNPs is required. To reveal the cytotoxicity and biocompatibility of PEG-UCNPs-5, cell cytotoxicity of PEG-UCNPs-5 in HeLa cells was measured using a 3-(4,5-dimethylthiazol-2-yl)-2,5 diphenyl-tetrazolium bromide (MTT) method. As shown in Figure S3 (Supporting Information), cell viability is beyond 90% when treated with 0–100 μg mL^{-1} PEG-UCNPs-5. Besides, cellular viability is still maintained at 78% when the concentration of nanoparticles is increased up to 1000 μg mL^{-1}. These results reveal that PEG-UCNPs-5 is suitable for the use as attractive bioprobes with the merit of low cytotoxicity.

2.3. In Vitro NIR-to-NIR UC Bioimaging

One important application of the remarkably enhanced NIR emission of PEG-UCNPs-5 is to develop new bioprobes for deep

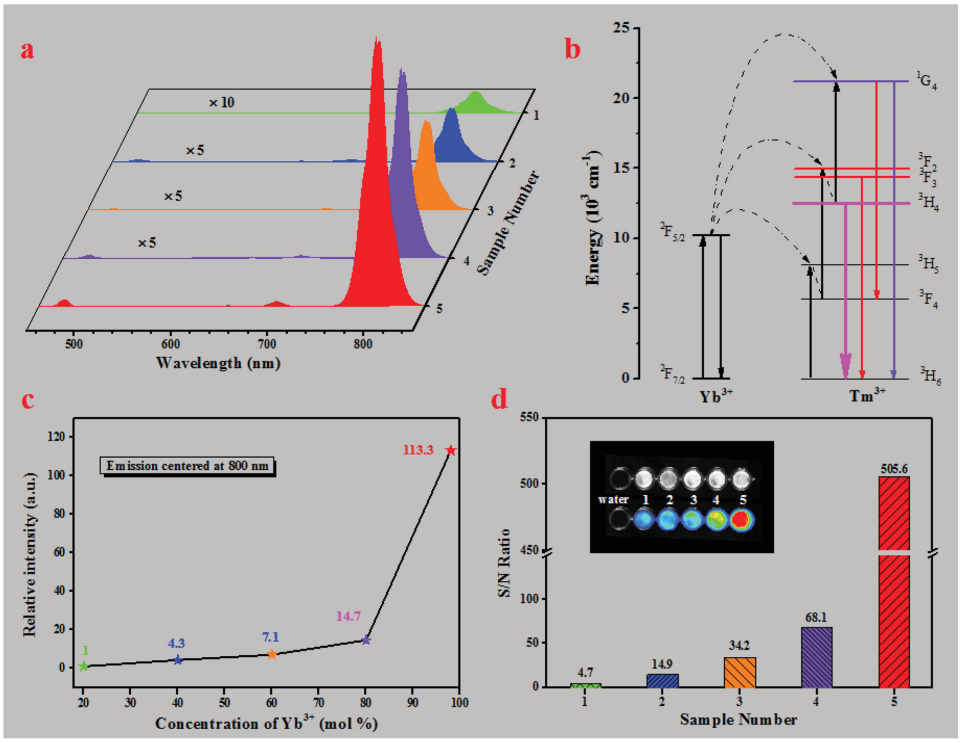

Figure 2. a) The emission spectra of PEG-UCNPs-1, -2, -3, -4, and -5, b) energy-level diagrams between Yb^{3+} and Tm^{3+} and proposed UC mechanisms under 980 nm excitation, c) The relative intensity of NIR emission centered at 800 nm of these UCNPs, and d) the calculated SNR based on the in vitro UC imaging of these UCNPs in 96-well plates. The insets in (d) indicate the corresponding bright field images (upper) and merged UC images (lower).

tissue bioimaging. In order to demonstrate the application, certain amounts of PEG-UCNPs-1, -3, and -5 were transferred into the pork muscles with different depths (3, 6, and 12 mm). As shown in **Figure 3**a, the UC signals of PEG-UCNPs-5 are visualized even at a depth of 12 mm. However, PEG-UCNPs-1 and -3 can only be detected at about 3 and 6 mm beneath the tissue. The calculated SNR (Figure 3b) reveals that PEG-UCNPs-5 presents the highest SNR values of 637.6 and 59.0 under 3 and 6 mm tissue surface, respectively, and maintains a high contrast of 15.8 even at a depth of 12 mm, indicating PEG-UCNPs-5 can be used as promising nanoprobes for in vivo deep tissue bioimaging. To further verify the advantage of NIR emission over visible emission, in vitro phantom experiment (Figure S4, Supporting Information) was performed using $NaYF_4$:Yb^{3+}/Er^{3+} UCNPs with green emission (545 nm) and PEG-UCNPs-5 with NIR emission (800 nm), respectively. As shown in Figure S4 (Supporting Information), $NaYF_4$:Yb^{3+}/Er^{3+} UCNPs with green emission present much lower penetration depths compared to PEG-UCNPs-5 with NIR emission. Therefore, NIR emission shows its unique advantage in deep tissue optical bioimaging.

To evaluate the capability of the in vivo UC optical bioimaging, a group of Kunming mice were subcutaneously injected with PEG-UCNPs-5. As demonstrated in Figure S5a (Supporting Information), no UC signal was detected in the mouse. After subcutaneous injection with PEG-UCNPs-5, intense UC emission signal (Figure S5b, Supporting Information) can be detected using a band pass filter at 809 nm with a bandwidth of 40 nm. To validate the feasibility of in vivo X-ray bioimaging, X-ray imaging model was executed using the same group of Kunming mice. As shown in Figure S6 (Supporting Information), there was no abnormal X-ray signal in the whole body of the mouse before injection with PEG-UCNPs-5. However, the injected site (Figure S6b, Supporting Information) exhibits high contrast properties of X-ray absorption.

The successful in vivo UC optical and X-ray bioimaging based on PEG-UCNPs-5 verifies their ability for each single bioimaging modality, and therefore we moved forward to access synergistic UC optical/X-ray bioimaging using PEG-UCNPs-5. Another Kunming mouse with subcutaneous injection of PEG-UCNPs-5 was used for evaluating the feasibility of the in vivo synergistic UC optical/X-ray bioimaging. Similar to the above bioimaging results, the non-injected mouse (Figure S7a, Supporting Information) showed no UC signal and obvious X-ray contrast. In contrast, the high-contrast X-ray (left panel in Figure S7b, Supporting Information) and intense UC signals (middle panel in Figure S7b, Supporting Information) were detected using the corresponding imaging system. Importantly, the X-ray signal matches well with the UC signal in the overlay image (right panel in Figure S7b, Supporting Information), indicating the successful synergistic dual-modal UC/X-ray bioimaging.

2.4. In Vivo Long-Circulation Tracking and Biodistribution

The UC optical imaging superiority using PEG-UCNPs-5 provides the possibility of long-lasting tracking of PEG-UCNPs-5 in vivo. To further validate the feasibility of the translocation

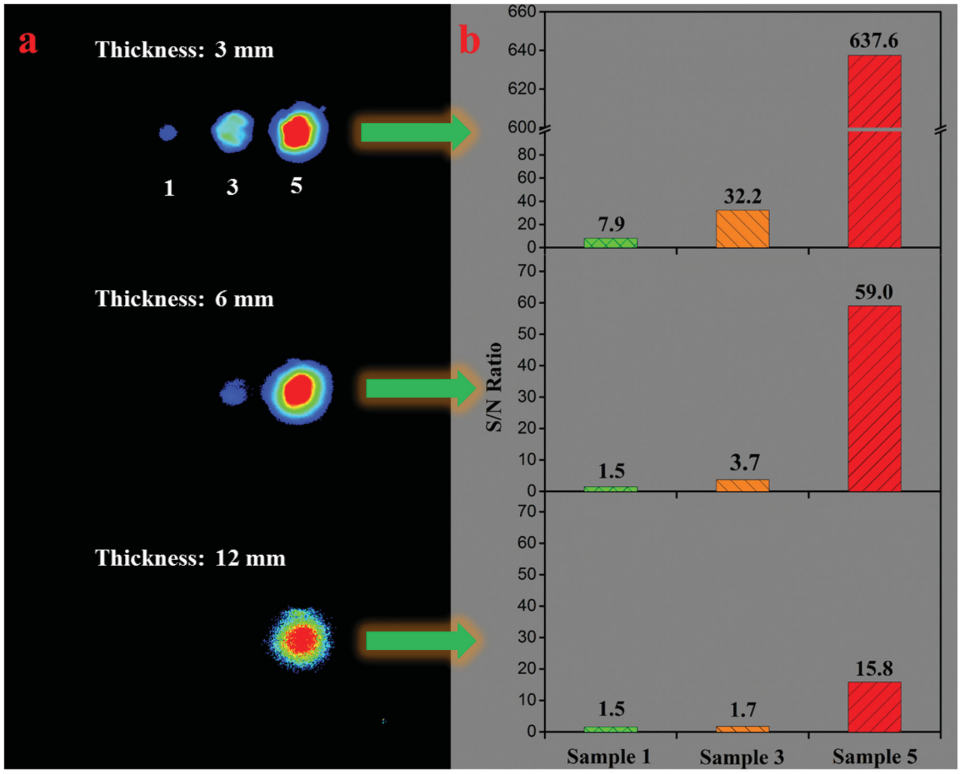

Figure 3. a) UC signal detection of pork muscle tissues treated with different nanoprobes (300 μL, 2 mg mL^{-1}): PEG-UCNPs-1, -3, and -5 in different depths (3, 6, and 12 mm). b) The corresponding SNR of these UCNPs.

and clearance of PEG-UCNPs-5 in the live mice, groups of Kunming mice were under intravenous injection of PEG-UCNPs-5 from tail vein. As shown in **Figure 4**a, UC signal in the live mouse was detected using the in vivo bioimaging system at different injection time intervals. UC signal was observed in the lungs location after 5 min injection and then gradually transferred into the liver location, which is consistent with our previous results.[45] As a result, UC signal in the liver region is gradually enhanced after injection. The corresponding statistical average value of UC signal in the lung location (Figure 4b) indicated that PEG-UCNPs-5 were firstly assembled in the lungs, increased to the maximum after 20 min injection. However, UC signal in the liver region (Figure 4c) increased after 4.5 h injection and showed a slight decrease trend subsequently.

It is expected that PEG-UCNPs-5 can be accumulated in the lung capillaries other than uptake by specific endothelial cells.[46] Figure S8 (Supporting Information) shows high-resolution X-ray bioimaging of Kunming mice dissected before and after 5 min intravenous injection of UCNPs-PEG-5 from tail vein. As demonstrated in Figure S8 (Supporting Information), it is obvious that the enhanced visualization of the blood vessels of the lungs is clearly observed after administration.

For the further study of translocation and excretion mechanism, these injected mice were dissected and the isolated organs (Figure 4d) were used for UC signal detection. The detected UC signals in the isolated lungs and the liver show the same variation trend when compared with that of in the live mouse. However, UC intensity in the isolated lungs is always higher than that in the liver, which is unmatched with the results of the live mouse. This is due to the different penetration depth of the emission light in the two locations in vivo and the exposure time (30 s for in vivo detection and 5 s for ex vivo detection). As shown in Figure 4d,e, weak UC signals were detected in the isolated kidney, stomach, and intestine after 20 min injection and presented the increase trend then. And, the feces of the live mouse after 1 h injection (Figure 4g) were collected and used for UC detection. The weak UC signal is presented. By contrast, the feces of the mouse before administration presented no UC signal. These results indicated that the excretion path of these nanoparticles was mainly ascribed to hepatobiliary excretion, which may provide a fundamental guide for the biological and pre-clinical applications.

2.5. In Vivo X-Ray CT Imaging

Apart from the excellent NIR emission, these Yb^{3+}-based UCNPs possess the large K-edge value and X-ray absorption coefficient, making these UCNPs promising contrast agents for X-ray CT imaging. To further demonstrate in vivo CT imaging, a mouse with intravenous injection from tail vein was detected using an X-ray micro-CT imaging system. As shown in **Figure 5**, there was no obvious signal from soft tissues before the injection of PEG-UCNPs-5. Predominant signal in the liver and spleen regions can be observed from the 3D volume-rendered CT images from the top and lateral view after 5 min intravenous injection of PEG-UCNPs-5. The CT contrast signals in these two locations increased with

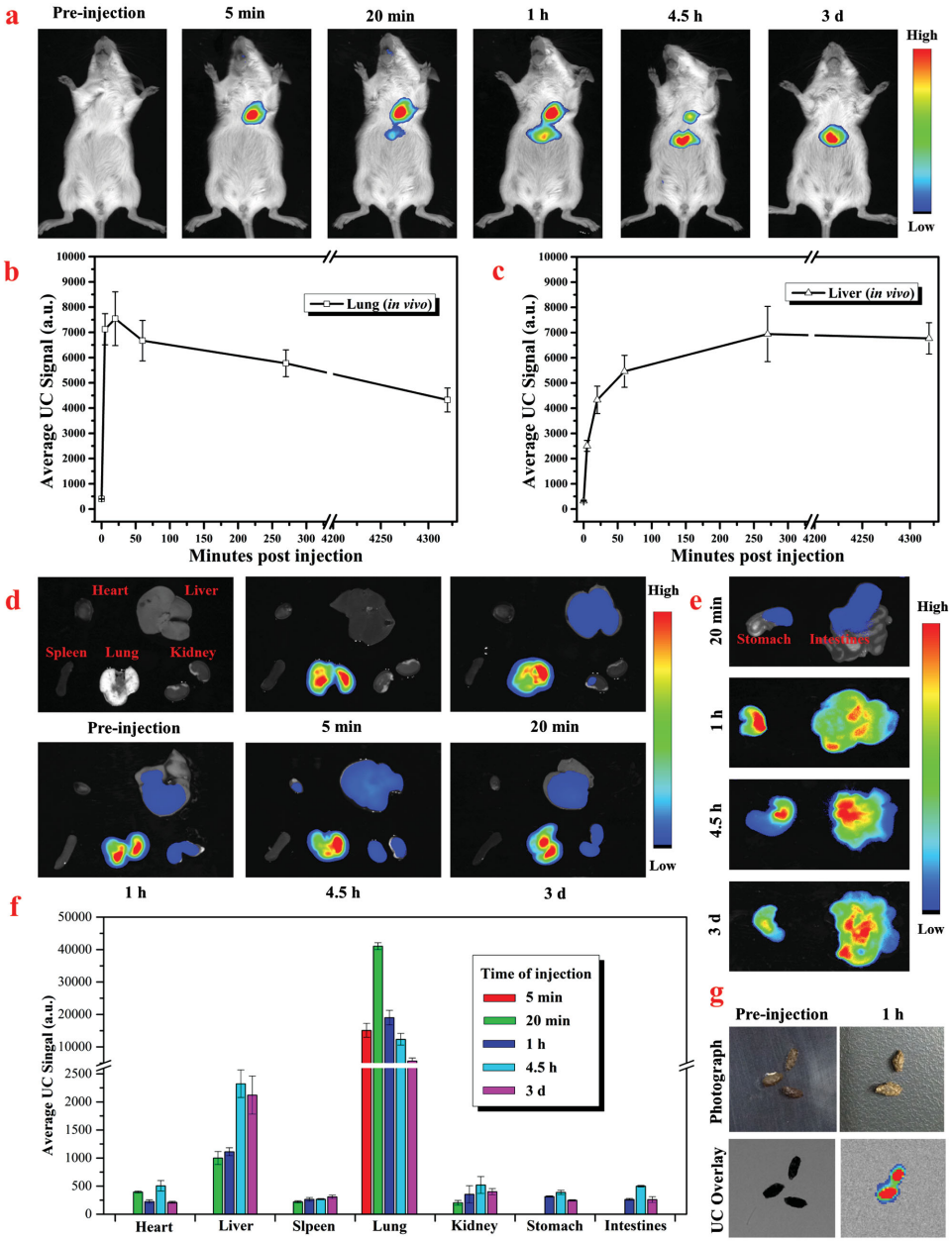

Figure 4. a) In vivo long-term tracking of PEG-UCNPs-5 based on UC optical bioimaging at different time periods, and quantification of UC optical signals from b) the lungs and c) the liver regions in the live mice. d,e) Biodistribution of PEG-UCNPs-5 in isolated organs (heart, liver, spleen, lung, kidney, stomach, and intestines) at well-designed intervals after injection from tail vein, f) quantification of UC optical signals from these organs, and g) digital photographs and UC optical imaging based on the feces of the live mouse after 1 h injection. The dosage of PEG-UCNPs-5 (2 mg mL^{-1}) is 50 μL for each mouse. Error bars for (b,c,f) and were based on three mice per group.

injection time. Particularly, the maximum values were reached in the liver and the spleen after 1 h and 1 d injection, respectively. These CT contrast results were different from aforementioned UC tracking using these nanoprobes, which was mainly ascribed to the injection dosage of nanoprobes and imaging accuracy between UC optical imaging and CT imaging. The high-contrast signals detected in the liver and spleen locations validate that PEG-UCNPs-5 can act as contrast agents for X-ray CT imaging.

2.6. In Vivo Detection of Small Tumors

To investigate the potential application of PEG-UCNPs-5 for in vivo tumor diagnosis, tumor-bearing mice intravenously injected PEG-UCNPs-5 probes via tail vein were used for in vivo UC luminescent bioimaging. As presented in **Figure 6**a, UC signal is initially concentrated in the lungs and liver regions after 1 h injection, which matches well with the above results of normal mice after intravenous injection of PEG-UCNPs-5.

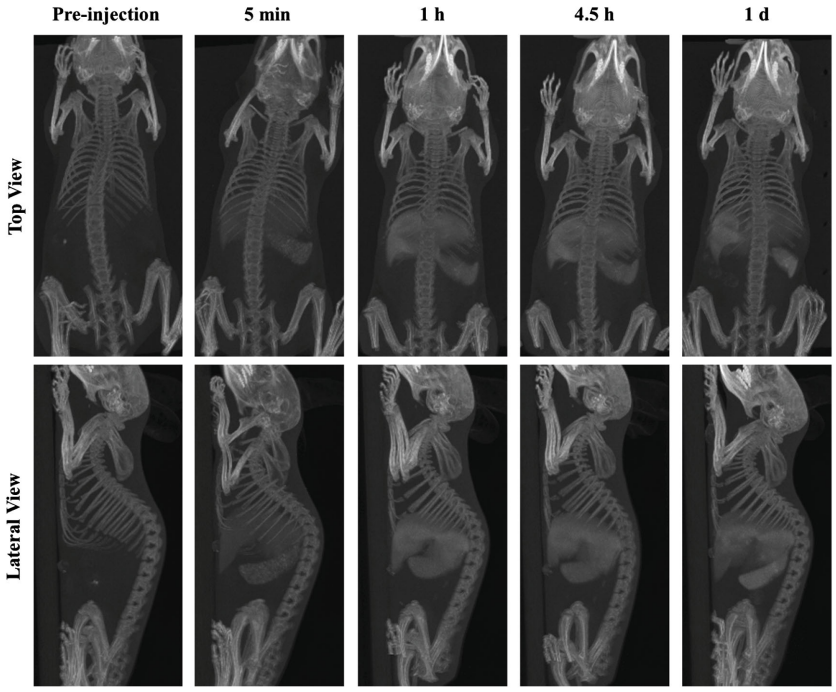

Figure 5. In vivo 3D volume-rendered CT imaging of a Kunming mouse before and after (5 min, 1 h, 4.5 h, and 1 d) intravenous injection of PEG-UCNPs-5 (200 μL, 20 mg mL^{-1}).

Importantly, the nanoprobes gradually transferred into the liver location and the tumor site after 3 h injection. As shown in Figure 6a,c, UC signal in tumor site increased until 12 h injection. Moreover, UC signal in tumor site with high contrast is still visualized after 24 h injection, revealing the feasibility of detecting tumor in vivo. To further demonstrate the small tumor detection, in situ (Figure 6b) and ex vivo (Figure 6d) UC images of the small tumor were carried out. Intense UC signal can be detected, further indicating the translocation of PEG-UCNPs-5 to tumor site which is likely due to the enhanced permeability and retention (EPR) effect of cancerous tumors.[47] These results indicate that PEG-UCNPs-5 can act as effective luminescent nanoprobes for tumor detection.

In addition to UC optical and CT imaging function, PEG-UCNPs-5 can also be used as contrast agents for T_2-weighted MRI. This is due to the fact that most of the paramagnetic lanthanide ions, such as Dy^{3+}, Ho^{3+} Tm^{3+}, Yb^{3+}, present short electronic transverse relaxation time, which affects T_2-weighted MRI.[38,40] The relaxation proton via a Curie mechanism largely affects T_2-weighted MRI,

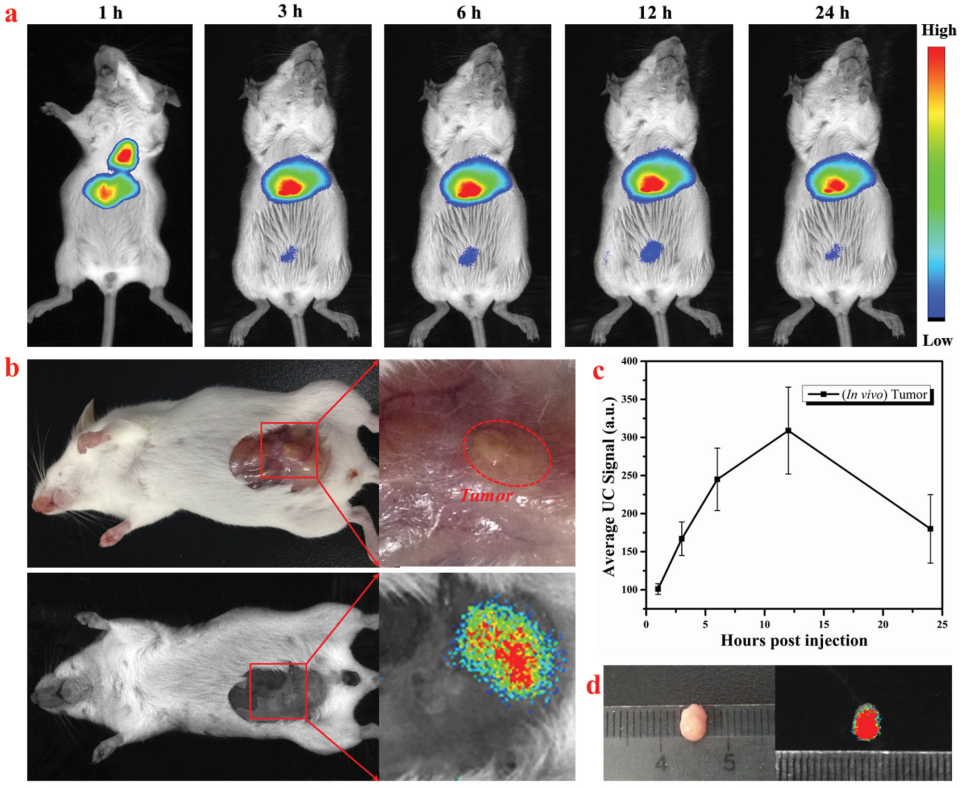

Figure 6. a) In vivo UC optical bioimaging of HeLa tumor-bearing mouse after intravenous injection with PEG-UCNPs-5 (50 μL, 2 mg mL^{-1}) at different time intervals. b) In situ digital photographs and UC images of the mouse. c) Average UC signal in a tumor site based on in vivo UC bioimaging. d) Digital photograph and ex vivo UC luminescence bioimaging of tumor. Error bars for (c) are based on three mice per group.

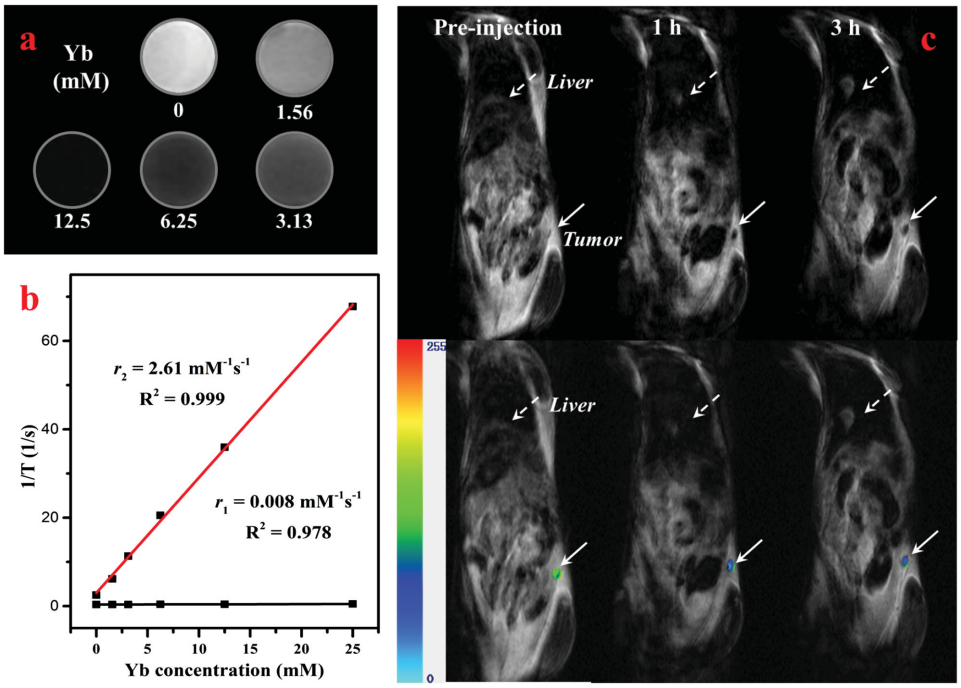

Figure 7. a) In vitro T_2-weighted MRI images of PEG-UCNPs-5 solutions with different Yb^{3+} concentrations, b) relaxation rate (1/T) versus Yb^{3+} molar concentration, and c) in vivo MRI coronal images of tumor-bearing mouse at different time points (pre-injection, 1 and 3 h) by intravenous injection of PEG-UCNPs-5 (50 μL, 2×10^{-3} M of Yb^{3+}). The dotted and full arrows in (c) refer to the high-contrast regions of the liver and tumor sites, respectively.

the contribution of which increases substantially with the external magnetic field and is proportional to the square of the effective magnetic moment of lanthanide ion.[38] Among them, Yb^{3+} ion has a relative short electronic relaxation time and high effective magnetic moment (μ_{eff} = 4.53 μ_B), which could generate efficient T_2 relaxation. However, the pure $NaYbF_4$ nanoparticles exhibit a limited T_2 contrast initially and a sharply enhanced contrast effects after 2 wt% of Ho^{3+} doping, while the enhancing mechanism is not clear and requires further study.[40] To validate the feasibility of PEG-UCNPs-5 as promising T_2-weighted contrast agents, in vitro T_2-weighted MRI was carried out using a 1.5 T Magnetom system. As illustrated in **Figure 7**a, T_2-weighted MRI images were gradually darker when the molar concentration of Yb^{3+} was increased in the range 0–12.5×10^{-3} M, indicating the remarkable dose-dependent negative enhancement effect. A further transverse relaxivity r_2 measurement was performed using the same concentration of the sample. As shown in Figure 7b, the relaxation rate r_2 ($1/T_2$) exhibits a good linear relationship versus Yb^{3+} molar concentration, and the calculated value based on fitting slop is 2.61 mM^{-1} s^{-1} using a 1.5 T Magnetom system. Contrast efficiency in T_2-weighted MRI is mainly ascribed to high r_2 values and r_2/r_1 ratio, and the higher the r_2/r_1 ratio, the better the imaging efficiency of the T_2 contrast agent.[48–50] Despite PEG-UCNPs-5 has relatively low transverse relaxivity (2.61 mM^{-1} s^{-1}) when compared with the clinically used T_2 contrast agents (such as, Resovist, Feridex, and Combidex; r_2/r_1 = 31, 22.6, and 6, respectively, measured at 3 T),[40,51,52] our designed Yb^{3+}-based PEG-UCNPs-5 possesses a high r_2/r_1 value of 326, which is larger than those of the clinical ones (Figure S9, Supporting Information). Therefore, it is expected that PEG-UCNPs-5 with high r_2/r_1 value can be used as high potential agent for T_2-weighted MRI. Most importantly, in vitro phantom and later in vivo T_2-MRI have demonstrated that our UCNPs can act as potential T_2-weighted MRI agents and even serve for T_2-weighted MRI guided small tumor detection.

With the high performance of PEG-UCNPs-5 on T_2-weighted MRI in vitro, small tumor detection based on T_2-weighted MRI in vivo was executed through intravenous injection of PEG-UCNPs-5. As presented in Figure 7c, high contrast in the liver region lasted over 3 h, which is coincident with the aforementioned results of long-lasting tracking of nanoparticles using normal mice and small tumor-bearing mice in vivo UC optical bioimaging. Interestingly, the high contrast was also observed in the tumor site after administration of PEG-UCNPs-5. To achieve a clear view of the negative enhancement effect, colored T_2-weighted MRI coronal images are also presented (Figure 7c), where the color of the tumor site changes from green to blue, corresponding to the T_2 signal variation from high to low level. As far as we know, this is the first time to demonstrate Yb^{3+}-based nanoprobes for T_2-weighted MRI guided small tumor detection, differing from the previously reported[53] Gd-based probes for tumor detection. Combined with the results of in vivo UC optical and CT bioimaging, PEG-UCNPs-5 can act as multifunctional nanoprobes for trimodal UC optical/CT/T_2-weighted MRI, and even UC optical and T_2-weighted MRI directed small tumor detection, providing an integrative platform for imaging-guided in vivo real-time detection and their early-stage diagnosis of small tumor in the future.

To further determine whether PEG-UCNPs-5 may induce any side effects or pathological changes, a long-term toxicity of PEG-UCNPs-5 was determined by testing the pathology

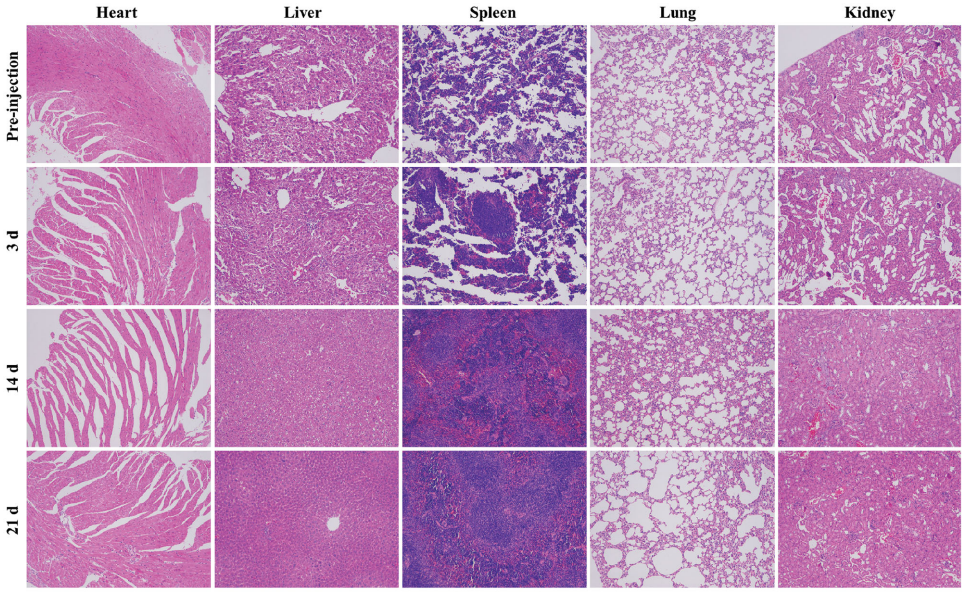

Figure 8. H&E-stained tissue sections images of heart, liver, spleen, lung and kidney collected from mice without injection and 3, 14, and 21 days after injection of PEG-UCNPs-5 (50 μL, 2 mg mL^{-1}). All images are shown at medium magnification (100×).

sections of major organs, including heart, liver, spleen, lung, and kidney (**Figure 8**). Healthy Kunming mice were dissected for 3, 14, and 21 d after intravenous injection of PEG-UCNPs-5 and the isolated organs were stained with hematoxylin and eosin (H&E). Compared with the control group, no noticeable sign of organ damage or inflammatory lesion of viscera tissues was observed. The results imply that PEG-UCNPs-5 should not induce apparent toxicity in the mouse, although these nanoparticles tend to retain in the body for a long time.

3. Conclusion

In this work, we report that the multifunctional PEGylated $NaYF_4$:Yb^{3+}/Tm^{3+} UCNPs nanoprobes synthesized by a simple one-pot hydrothermal reaction can be effectively used for the early-stage diagnosis of small tumor via in vivo tri-modal NIR-to-NIR UC optical/CT/T_2-weighted MRI imaging techniques. PEG-UCNPs-5 takes advantage of dramatically enhanced NIR emission and PEG coating for in vivo long-circulation tracking and translocation of nanoparticles based on UC optical imaging. PEG-UCNPs-5 can act as ideal luminescent probes for UC optical bioimaging and high-contrast agents for CT and T_2-weighted MRI. Significantly, PEG-UCNPs-5 can be used for real-time detection of small tumor and acted as excellent tumor-diagnosis nanoprobes under both NIR-to-NIR UC optical and T_2-weighted MRI imaging modalities. The measurement of long-term toxicity of PEG-UCNPs-5 indicates little side effect or pathological change by testing the pathology sections of major organs (heart, liver, spleen, lung, and kidney). These results make PEG-UCNPs-5 promising probe for multimodal deep tissue bioimaging and disease detection, especially for early-stage cancer diagnosis.

4. Experimental Section

Chemicals and Materials: The oxides Y_2O_3 (99.99%), Yb_2O_3 (99.99%), and Tm_2O_3 (99.99%) were obtained from Sigma–Aldrich. The corresponding nitrates $Y(NO_3)_3$, $Yb(NO_3)_3$, and $Tm(NO_3)_3$ were synthesized by adding oxides into dilute HNO_3 solution. PEG ($M_w \approx 5000$), ethylene glycol (EG), NaF, NaOH, and other reagents bought from Sinopharm Chemical Reagent Co., China were of analytical grade. All chemicals were used as received without further purification.

Synthesis of PEGylated UCNPs: A simple one-pot hydrothermal route was used to synthesize the hydrophilic PEGylated $NaYF_4$:x%Yb^{3+}/2%Tm^{3+} (x = 20, 40, 60, 80, and 98) UCNPs.[45] 1.0 g of PEG was added into 15 mL of EG to form a clear mixture under agitation. And then, total amounts (1 mmol) of rare earth nitrides were dissolved into the aforementioned solution. After another 20 min stirring, 5 mL of EG and 4 mL of NaF (1 M) aqueous solution were added. After 30 min stirring, the homogeneous solution was transferred into a 50 mL stainless steel autoclave. The vessel was sealed and maintained at 190 °C for 24 h. The products were cooled naturally to room temperature. The precipitates in the bottom of the vessel were washed with ethanol and deionized water three times and collected via centrifugation. Aqueous solution containing UCNPs with designed concentration was prepared for further use. To verify the surface coating of PEGylated UCNPs, the control experiments using the similar method were conducted. The replacement of EG and PEG by DI water was executed in the fabrication of UCNPs without PEG coating.

Characterization: XRD data of PEG-UCNPs-1, -3, and -5 were recorded via a Rigaku 2500 X-ray diffractometer using a D/max-γA system with Cu-Kα radiation (λ = 1.5406 Å) at 40 kV and 250 mA. All these PEGylated UCNPs were characterized by FE-SEM (FEI NanoSEM 450), TEM (JEOL-2100F), HR-TEM, and SAED. The EDS analysis was performed under TEM assay. The surface ligands of PEG-UCNPs-5 and UCNPs without PEG coating were detected via FTIR spectra using a Magna 760 spectrometer (Nicolet). UC emission spectra of these UCNPs were detected by a Zolix analytical instrument (fluoroSENS 9000A) equipped with external 980 nm laser as excitation light source.

Cytotoxicity Assay: The cell toxicity of PEG-UCNPs-5 was detected by an MTT proliferation assay method in HeLa cells. HeLa cells were cultured in Dulbecco's modified Eagle medium (DMEM, 10% fetal

bovine serum +1% penicillin/streptomycin) at 37 °C and 5% CO_2. Approximate 5×10^4 cells per well were plated in 96-well plates. Designed concentrations of PEG-UCNPs-5 (0, 100, 250, 500, and 1000 μg mL^{-1}) were added into the cells in the absence of serum after 24 h incubation. 20 μL of MTT solution was added after 4 h incubation. Blue formazan crystals were detected by microscope. Media were removed and then 150 μL of DMSO was added per well. The absorbance (Abs.) was measured using a microtiter plate reader. The cell viability (%) was then calculated as [Abs.490 (treated cells)-background]/[Abs.490 (untreated cells)-background] × 100%.

UC Optical/X-ray Bioimaging: All of these PEGylated UCNPs with the same concentration (2 mg mL^{-1}) were transferred into 96-well plates (300 μL per well), respectively. In vitro UC optical bioimaging was detected using a multimodal in vivo imaging system (Bruker In Vivo FX PRO) equipped with external 980 nm laser as light source. UC signals were collected through the band pass filter (809/20 nm). PEG-UCNPs-1, -3, and -5 (2 mg mL^{-1}, 300 μL per well) were placed into pork muscle tissues at various depths (3, 6, 12 mm). The value of SNR was calculated using the average value of UC signal on each site of UCNPs dividing the background signal. For in vivo imaging, Kunming mice (three per group) were anesthetized by intraperitoneal injection using 150 μL of pentobarbital sodium aqueous solution (10 wt%). And then, 50 μL of aqueous solution containing PEG-UCNPs-5 (2 mg mL^{-1}) was subcutaneously injected into the mice. In vivo UC optical and X-ray bioimaging were captured using the same imaging system. All animal procedures comply with the institutional animal use and care regulations approved by the Laboratory Animal Center of Hunan Province.

CT Bioimaging: To investigate in vivo CT imaging based on PEG-UCNPs-5, three mice were anesthetized through intraperitoneal injection with 150 μL of pentobarbital sodium solution (10 wt%). After that, 200 μL of aqueous solutions containing PEG-UCNPs-5 (20 mg mL^{-1}) were injected into each of these mice via intravenous injections from tail vein. CT images were captured before injection and after 5 min, 1 h, 6 h, 12 h, and 1 d injection employing a multimodal imaging system (Optical Multimodality Molecular Imaging System for Small Animal, Key Laboratory of molecular Imaging, CAS). The imaging was executed as following parameters: thickness, 120 μm; base resolution, 120 × 120 $μm^2$; 40 kV, 0.8 mA. The 3D renderings of in vivo CT images were analyzed with 3D Med 4.6 Software.

In Vivo Long-Term Tracking Based on UC Optical Bioimaging: To investigate in vivo whole body biodistribution of PEG-UCNPs-5, some groups of Kunming mice were intravenously injected 50 μL of PEG-UCNPs-5 aqueous solution (2 mg mL^{-1}) from tail vein. Bright field images and UC optical images at different time intervals were captured in sequence under the multi-modal in vivo imaging system. To further investigate the biodistribution and accumulation of PEG-UCNPs-5 in various organs, these injected Kunming mice were sacrificed at designed intervals and the major organs of these dissected mice (including heart, liver, spleen, lung, kidney, stomach, and intestines) were also used to detect bright field images and UC optical images.

UC Optical Bioimaging-Directed Tumor Detection: HeLa cells (1×10^7 cells per site) were implanted into BALB/C mice by subcutaneous injection. In vivo tumor imaging was performed when tumor reached 3–5 mm in average diameter (6–8 d after implant). These inoculated tumor modals (3 per group) were anesthetized by intraperitoneal injection using 150 μL of pentobarbital sodium aqueous solution (10 wt%). 50 μL of aqueous solution containing PEG-UCNPs-5 (2 mg mL^{-1}) was then intravenously injected into these mice. UC signal images were captured at regular time intervals. The in situ/ex vivo imaging was executed by the same parameters. The corresponding digital pictures were taken with a Canon digital camera.

T_2-Weighted MRI In Vitro and In Vivo: To prove the feasibility of PEG-UCNPs-5 as contrast agents for T_2-weighted MRI, in vitro T_2-weighted MRI was measured. PEG-UCNPs-5 solutions with certain Yb^{3+} concentrations (0×10^{-3}, 1.56×10^{-3}, 3.13×10^{-3}, 6.25×10^{-3}, and 12.5×10^{-3} M) were dispersed in 1.0 mL tubes. Relaxivity values were measured by the curve fitting of $1/T_2$ versus Yb^{3+} concentration. T_2-weighted MRI images were acquired using 1.5 T Magnetom system (HT-MRSI65-35, Shanghai Shinning Global Scientific and Educational Equipment Co.) using T_2-weighted sequence as follows: Spin Echo (SE), TR = 500 ms, TE = 65 ms, matrix = 512 × 256, FOV = 50 × 130, slice thickness = 0.5 mm. In vivo tumor detection experiments were performed via intravenously injecting 50 μL of PEG-UCNPs-5 solution with 2×10^{-3} M of Yb^{3+} concentration into an anesthetic mouse with small tumor using 1.2 T Magnetom system (HT-ANNMR-50, Shanghai Shinning Global Scientific and Educational Equipment Co.). Coronal cross-sectional images were captured before and after administration.

Histological Assessment: 50 μL of PEG-UCNPs-5 (2 mg mL^{-1}) was intravenously injected into Kunming mice and the untreated mice selected as control group. Major organs (heart, liver, spleen, lung, and kidney) were isolated from mice of control and experimental groups after 3, 14, and 21 d. All these tissues were H&E-stained to observe histological changes. The histological sections were operated using an optical microscope.

Supporting Information

Supporting Information is available from the Wiley Online Library or from the author.

Acknowledgements

This work was supported by the National Natural Science Foundation of China (Nos. 51102202, and 31370736), Specialized Research Fund for the Doctoral Program of Higher Education of China (No. 20114301120006) and Hunan Provincial Natural Science Foundation of China (No. 12JJ4056), Scientific Research Fund of Hunan Provincial Education Department (13B062), and CAS/SAFEA International Partnership Program for Creative Research Teams. The authors thank Dr. Hui Hui in Key Laboratory of molecular Imaging, Chinese Academy of Sciences for CT bioimaging and helpful discussions.

Received: August 30, 2015
Revised: September 20, 2015
Published online: October 31, 2015

[1] J. Zhou, Z. Liu, F. Y. Li, *Chem. Soc. Rev.* **2012**, *41*, 1323.
[2] X. Chen, W. Xu, L. H. Zhang, X. Bai, S. B. Cui, D. L. Zhou, Z. Yin, H. W. Song, D. H. Kim, *Adv. Funct. Mater.* **2015**, *25*, 5462.
[3] Y. S. Liu, D. T. Tu, H. M. Zhu, X. Y. Chen, *Chem. Soc. Rev.* **2013**, *42*, 6924.
[4] N. M. Idris, M. K. Gnanasammandhan, J. Zhang, P. C. Ho, R. Mahendran, Y. Zhang, *Nat. Med.* **2012**, *18*, 1580.
[5] L. Cheng, C. Wang, L. Z. Feng, K. Yang, Z. Liu, *Chem. Rev.* **2014**, *114*, 10869.
[6] F. Wang, Y. Han, C. S. Lim, Y. H. Lu, J. Wang, J. Xu, H. Y. Chen, C. Zhang, M. H. Hong, X. G. Liu, *Nature* **2010**, *463*, 1061.
[7] Z. Yin, Y. S. Zhu, W. Xu, J. Wang, S. Xu, B. Dong, L. Xu, S. Zhang, H. W. Song, *Chem. Commun.* **2013**, *49*, 3781.
[8] P. Huang, W. Zheng, S. Y. Zhou, D. T. Tu, Z. Chen, H. M. Zhu, R. F. Li, E. Ma, M. D. Huang, X. Y. Chen, *Angew. Chem. Int. Ed.* **2014**, *53*, 1252.
[9] W. Zheng, P. Huang, D. T. Tu, E. Ma, H. M. Zhu, X. Y. Chen, *Chem. Soc. Rev.* **2015**, *44*, 1379.
[10] M. He, P. Huang, C. L. Zhang, H. Y. Hu, C. C. Bao, G. Gao, R. He, D. X. Cui, *Adv. Funct. Mater.* **2011**, *21*, 4470.
[11] Z. G. Yi, W. Lu, H. R. Liu, S. J. Zeng, *Nanoscale* **2015**, *7*, 542.
[12] M. K. Tsang, G. X. Bai, J. H. Hao, *Chem. Soc. Rev.* **2015**, *44*, 1585.

[13] Z. G. Yi, S. J. Zeng, W. Lu, H. B. Wang, L. Rao, H. R. Liu, J. H. Hao, *ACS Appl. Mater. Interfaces* **2014**, *6*, 3839.
[14] Z. Chen, W. Zheng, P. Huang, D. T. Tu, S. Y. Zhou, M. D. Huang, X. Y. Chen, *Nanoscale* **2015**, *7*, 4274.
[15] Y. H. Zhang, L. X. Zhang, R. R. Deng, J. Tian, Y. Zong, D. Y. Jin, X. G. Liu, *J. Am. Chem. Soc.* **2014**, *136*, 4893.
[16] J. C. Boyer, F. Vetrone, L. A. Cuccia, J. A. Capobianco, *J. Am. Chem. Soc.* **2006**, *128*, 7444.
[17] B. Dong, S. Xu, J. Sun, S. Bi, D. Li, X. Bai, Y. Wang, L. P. Wang, H. W. Song, *J. Mater. Chem.* **2011**, *21*, 6193.
[18] J. Wang, F. Wang, C. Wang, Z. Liu, X. G. Liu, *Angew. Chem., Int. Ed.* **2011**, *50*, 10369.
[19] D. K. Chatteriee, A. J. Rufalhah, Y. Zhang, *Biomaterials* **2008**, *29*, 937.
[20] D. M. Yang, P. A. Ma, Z. Y. Hou, Z. Y. Cheng, C. X. Li, J. Lin, *Chem. Soc. Rev.* **2015**, *44*, 1416.
[21] W. Zheng, D. T. Tu, P. Huang, S. Y. Zhou, Z. Chen, X. Y. Chen, *Chem. Commun.* **2015**, *51*, 4129.
[22] Q. F. Xiao, X. P. Zheng, W. B. Bu, W. Q. Ge, S. J. Zhang, F. Chen, H. Y. Xing, Q. G. Ren, W. P. Fan, K. L. Zhao, Y. Q. Hua, J. L. Shi, *J. Am. Chem. Soc.* **2013**, *135*, 13041.
[23] S. J. Zeng, H. B. Wang, W. Lu, Z. G. Yi, L. Rao, H. R. Liu, J. H. Hao, *Biomaterials* **2014**, *35*, 2934.
[24] X. Bai, D. Li, Q. Liu, B. Dong, S. Xu, H. W. Song, *J. Mater. Chem.* **2012**, *22*, 24698.
[25] P. Du, L. H. Luo, W. P. Li, Q. Y. Yue, H. B. Chen, *Appl. Phys. Lett.* **2014**, *104*, 152902.
[26] M. Wang, C. C. Mi, W. X. Wang, C. H. Liu, Y. F. Wu, Z. R. Xu, C. B. Mao, S. K. Xu, *ACS Nano* **2009**, *3*, 1580.
[27] S. J. Zeng, M. K. Tsang, C. F. Chan, K. L. Wong, B. Fei, J. H. Hao, *Nanoscale* **2012**, *4*, 5118.
[28] R. Naccache, F. Vetrone, V. Mahalingam, L. A. Cuccia, J. A. Capobianco, *Chem. Mater.* **2009**, *21*, 717.
[29] Z. G. Yi, T. M. Zeng, Y. R. Xu, W. Lu, C. Qian, H. R. Liu, S. J. Zeng, J. H. Hao, *Nanotechnology* **2015**, *26*, 385702.
[30] G. Tian, Z. J. Gu, L. J. Zhou, W. Y. Yin, X. X. Liu, L. Yan, S. Jin, W. L. Ren, G. M. Xing, S. J. Li, Y. L. Zhao, *Adv. Mater.* **2012**, *24*, 1226.
[31] S. J. Zeng, Z. G. Yi, W. Lu, C. Qian, H. B. Wang, L. Rao, T. M. Zeng, H. R. Liu, H. J. Liu, B. Fei, J. H. Hao, *Adv. Funct. Mater.* **2014**, *24*, 4051.
[32] G. Y. Chen, T. Y. Ohulchanskyy, R. Kumar, H. Ågren, P. N. Prasad, *ACS Nano* **2010**, *4*, 3163.
[33] J. Zhou, Y. Sun, X. X. Du, L. Q. Xiong, H. Hu, F. Y. Li, *Biomaterials* **2010**, *31*, 3287.
[34] S. B. Yu, A. D. Watson, *Chem. Rev.* **1999**, *99*, 2353.
[35] J. H. Hubbell, S. M. Seltzer, *Tables of X-Ray Mass Attenuation Coefficients and Mass Energy-Absorption Coefficients* [Online], September 17, 2009, http://physics.nist.gov/PhysRefData/XrayMassCoef/(accessed: May 2015).
[36] D. Pan, E. Roessl, J. P. Schlomka, S. D. Caruthers, A. Senpan, M. J. Scott, J. S. Allen, H. Zhang, G. Hu, P. J. Gaffney, E. T. Choi, V. Rasche, S. A. Wickline, R. Proksa, G. M. Lanza, *Angew. Chem. Int. Ed.* **2010**, *49*, 9635.
[37] Y. L. Liu, K. L. Ai, J. H. Liu, Q. H. Yuan, Y. Y. He, L. H. Lu, *Angew. Chem. Int. Ed.* **2012**, *51*, 1437.
[38] S. Viswanathan, Z. Kovacs, K. N. Green, S. J. Ratnakar, A. D. Sherry, *Chem. Rev.* **2010**, *110*, 2960.
[39] F. Chen, W. B. Bu, S. J. Zhang, X. H. Liu, J. N. Liu, H. Y. Xing, Q. F. Xiao, L. P. Zhou, W. J. Peng, L. Z. Wang, J. L. Shi, *Adv. Funct. Mater.* **2011**, *21*, 4285.
[40] D. L. Ni, W. B. Bu, S. J. Zhang, X. P. Zheng, M. Li, H. Y. Xing, Q. F. Xiao, Y. Y. Liu, Y. Q. Hua, L. P. Zhou, W. J. Peng, K. L. Zhao, J. L. Shi, *Adv. Funct. Mater.* **2014**, *24*, 6613.
[41] M. Bottrill, L. Kwok, N. J. Long, *Chem. Soc. Rev.* **2006**, *35*, 557.
[42] T. Y. Cao, Y. Yang, Y. Sun, Y. Q. Wu, Y. Gao, W. Feng, F. Y. Li, *Biomaterials* **2013**, *34*, 7127.
[43] S. H. Huang, J. Xu, Z. G. Zhang, X. Zhang, L. Z. Wang, S. L. Gai, F. He, N. Niu, M. L. Zhang, P. P. Yang, *J. Mater. Chem.* **2012**, *22*, 16136.
[44] H. T. Wong, H. L. W. Chan, J. H. Hao, *Opt. Express* **2010**, *18*, 6123.
[45] Z. G. Yi, W. Lu, Y. R. Xu, J. Yang, L. Deng, C. Qian, T. M. Zeng, H. B. Wang, L. Rao, H. R. Liu, S. J. Zeng, *Biomaterials* **2014**, *35*, 9689.
[46] B. Wang, X. He, Z. Y. Zhang, Y. L. Zhao, W. Y. Feng, *Acc. Chem. Res.* **2013**, *46*, 761.
[47] L. Cheng, K. Yang, Y. G. Li, J. H. Chen, C. Wang, M. W. Shao, S. T. Lee, Z. Liu, *Angew. Chem. Int. Ed.* **2011**, *50*, 7385.
[48] J. Qin, S. Laurent, Y. S. Jo, A. Roch, M. Mikhaylova, Z. M. Bhujwalla, R. N. Muller, M. Muhammed, *Adv. Mater.* **2007**, *19*, 2411.
[49] E. Terreno, D. D. Castelli, A. Viale, S. Aime, *Chem. Rev.* **2010**, *110*, 3019.
[50] G. K. Das, N. J. J. Johnson, J. Cramen, B. Blasiak, P. Latta, B. Tomanek, F. C. J. M. van Veggel, *J. Phys. Chem. Lett.* **2012**, *3*, 524.
[51] M. Rohrer, H. Bauer, J. Mintorovitch, M. Requardt, H. J. Weinmann, *Invest. Radiol.* **2005**, *40*, 715.
[52] Y. X. J. Wang, *Quant. Imaging Med. Surg.* **2011**, *1*, 35.
[53] C. Y. Liu, Z. Y. Gao, J. F. Zeng, Y. Hou, F. Fang, Y. L. Li, R. R. Qiao, L. Shen, H. Lei, W. S. Yang, M. Y. Gao, *ACS Nano* **2013**, *7*, 7227.